Article

Synthesis of Flower-like ZnO and Its Enhanced Sensitivity towards NO₂ Gas Detection at Room Temperature

Zhicheng Cai [1], Jiho Park [2] and Sunghoon Park [3,4,*]

1 Department of Software Convergence, Sejong University, 209 Neungdong-ro, Gwangjin-gu, Seoul 05006, Republic of Korea; cai1121@hotmail.com
2 Department of Electronics and Information Engineering, Sejong University, 209 Neungdong-ro, Gwangjin-gu, Seoul 05006, Republic of Korea; jjpjh5483@naver.com
3 Department of Intelligent and Mechatronics Engineering, Sejong University, 209 Neungdong-ro, Gwangjin-gu, Seoul 05006, Republic of Korea
4 Department of Semiconductor System Engineering, Sejong University, 209 Neungdong-ro, Gwangjin-gu, Seoul 05006, Republic of Korea
* Correspondence: s.park@sejong.ac.kr; Tel.: +82-2-6935-2522

Abstract: A flower-like ZnO was successfully synthesized via a simple chemical precipitation method at room temperature (RT) in distilled water, without the use of any catalysts or substrates. The sample's structure was analyzed using various techniques including scanning electron microscopy (SEM), X-ray diffraction (XRD), transmission electron microscopy (FETEM), and X-ray photoelectron spectroscopy (XPS), which confirmed its hexagonal structure. UV–visible optical absorption measurements also revealed the presence of UV absorption at 365 nm. A reasonable growth mechanism for the formation of flower-like ZnO was proposed based on these analyses. The response of the sample to low concentrations of NO₂ (1 ppm) was evaluated at different calcination temperatures, and the results showed that the best response was achieved when the sample was calcined at 600 °C. The flower-like ZnO sample labeled as 6ZnO showed the highest response of 54.18 when exposed to 1 ppm of NO₂ gas at RT. Additionally, 6ZnO exhibited good response and recovery properties of 11 s and 93 s, respectively, at low concentrations of NO₂ at 1 ppm. The gas sensing mechanism and the mechanism of the enhanced gas response of the flower-like ZnO are discussed.

Keywords: ZnO; NO₂ gas sensor; metal oxide semiconductor; room temperature

1. Introduction

Among the various environmental pollutants released from industrial production and automobile emissions, nitrogen dioxide (NO₂) is considered the most hazardous air pollutant. Even low levels of NO₂ in the parts per billion (ppb) range can be harmful to human health, underscoring the urgent need for NO₂ monitoring tools accessible to the public [1–4]. To meet this need, portable, fast-response sensors that are small, robust, have long lifetimes, and exhibit high sensitivity and fast response times are necessary. Additionally, low power consumption and compatibility with wearable devices can enhance their utility and usability. Much research in recent years has focused on NO₂ sensors operated at RT [5–8]. However, these RT sensors generally suffer from slow response, poor reversibility, and insufficient sensitivity. The use of ultraviolet (UV) illumination has gained significant interest as an inexpensive and straightforward method to enhance the sensitivity, response, reversibility, and selectivity of NO₂ sensors. Despite this, many reported UV-activated NO₂ sensors based on nanostructured metal oxide semiconductors (MOS) still exhibit suboptimal performance at room temperature for practical applications [9–12].

Zinc oxide (ZnO) has become an attractive candidate in the field of gas sensing due to its low cost, facile fabrication, and excellent sensing properties. ZnO possesses a wide bandgap (3.37 eV) and has been realized for a variety of applications, including gas sensors,

photovoltaic purification, and transparent conducting oxide electrodes. ZnO is considered an ideal semiconductor for NO_2 gas sensors. Although ZnO has been used in conventional MOS gas sensors, issues related to low selectivity and high operating temperature remain as limitations that hinder its practical applications [13–21]. Numerous studies have focused on enhancing the sensing properties of ZnO through various approaches. One such approach involves modifying ZnO with noble metals like Pt, Pd, Au, or Ag. These noble metal modifications aim to improve the sensor's performance by enhancing its catalytic activity and surface reactivity towards target gases. Another strategy involves engineering ZnO into nanostructures with diverse morphologies, such as nanowires, nanorods, or nanoparticles. These nanostructured ZnO materials offer increased surface-to-volume ratios, promoting gas adsorption and facilitating electron transfer, thereby enhancing sensing performance. Moreover, the formation of p–n or n–n heterojunctions with alternate metal-oxide-semiconductor (MOS) layers has been explored to enhance the gas sensing properties of ZnO. These heterojunctions create favorable electron and hole transport pathways, enabling efficient charge separation and promoting gas molecule adsorption. These innovative approaches have shown promising results in improving the selectivity, sensitivity, and response/recovery times of ZnO-based gas sensors. Recent studies have also focused on refining the preparation methods and modifying the morphologies of nanostructured ZnO-based gas sensors. These advancements have led to significant improvements in sensing performance [22–25]. For instance, controlled synthesis techniques and precise tuning of morphological parameters, such as grain size and porosity, have been employed to optimize the sensor's surface area, increase gas adsorption sites, and enhance electron depletion layer (EDL) formation. The EDL, which plays a crucial role in the sensor's performance, can be increased by manipulating the grain size, porosity, and surface state of ZnO. These factors contribute to the overall sensitivity and selectivity of the sensor.

Simply reducing the grain size of a material may not necessarily lead to improved gas-sensing performance. In fact, excessively small grain sizes may promote particle agglomeration and result in reduced exposed specific surface area. Thus, achieving a balance between optimal grain size, preventing material agglomeration, promoting gas diffusion, and their synergistic effects is crucial for achieving a low-operating temperature gas response [26,27]. Surface defects, such as oxygen vacancies, are crucial for the gas sensing performance of ZnO nanostructures. These vacancies serve as active sites for gas-sensing reactions, leading to enhanced gas adsorption, dissociation, and subsequent redox reactions. The presence of oxygen vacancies in ZnO nanostructures significantly influences their gas sensing capabilities. These vacancies are created when oxygen atoms are missing from the crystal lattice, leaving behind unpaired electrons. These unpaired electrons make the oxygen vacancies highly reactive and provide binding sites for gas molecules. When a gas molecule comes into contact with the surface of ZnO nanostructures, it can adsorb onto the oxygen vacancies. The presence of oxygen vacancies increases the adsorption capacity of ZnO, allowing more gas molecules to be captured on the surface. This enhanced gas adsorption leads to an increased sensitivity of ZnO nanostructures towards gas detection. Furthermore, the gas molecule adsorbed on the oxygen vacancy can undergo dissociation. The high reactivity of the oxygen vacancy facilitates the breaking of chemical bonds within the gas molecule, leading to the formation of reactive species. These reactive species can then participate in subsequent redox reactions with other gas molecules or with the ZnO surface. The redox reactions involving the gas molecules and the oxygen vacancies result in changes in the electrical and optical properties of the ZnO nanostructures. These changes can be measured and quantified, providing a means to detect and quantify the presence of the target gas [28,29]. UV illumination has the ability to generate photocurrents and increase the conductivity of n-type metal oxides. Additionally, it can improve the surface activity of ZnO and increase its carrier density, leading to enhanced sensing performance. Thus, the optoelectronic properties of n-type metal oxide nanostructures play a crucial role in their UV-activated NO_2 sensing properties. Several studies have demonstrated

improved NO_2 sensing performance under UV illumination by tuning the optoelectronic properties of metal oxide nanostructures [30,31].

In this study, we employed a simple chemical precipitation method to synthesize flower-like ZnO at room temperature, using distilled water without any capping agents or catalysts. The as-obtained flower-like ZnO was able to detect ppb-level NO_2 gas at room temperature under 365 nm blue–violet laser irradiation with a power of 80 mW/cm^2. The surface morphologies, phase compositions, surface chemical states, optical characteristics, and sensing properties were thoroughly investigated. Based on the experimental results, we proposed a gas sensing mechanism to explain the performance of the sensor.

2. Materials and Methods

2.1. Materials

Zinc nitrate hexahydrate ($Zn(NO_3)_2 \cdot 6H_2O$, 99%) was purchased from Alfa Aesar (Thermo Fisher Scientific, Ward Hill, MA 01835, USA). Sodium hydroxide beads (NaOH) were purchased from Daejung Chemicals & Metals Co., Ltd. (Siheung-si, Republic of Korea). All chemicals used in the experiment were of analytical grade and were used without further purification.

2.2. Synthesis of Flower-like ZnO

The synthesis process is illustrated in Figure 1a. To synthesize flower-like ZnO, 1.5 g of zinc nitrate hexahydrate ($Zn(NO_3)_2 \cdot 6H_2O$) and 0.9 g of sodium hydroxide (NaOH) were dissolved in 50 mL of distilled water under stirring for 30 min, and then left to cool down to RT. The resulting white precipitate was separated by centrifugation, washed with distilled water and absolute alcohol several times to remove any possible residues. Then, it was calcined at high temperature using a tube furnace in atmospheric conditions to synthesize the final samples. The sample without any calcination process was labelled as 0ZnO, and other samples, which calcined at 400, 600, and 800 °C for 2 h, were labelled as 4ZnO, 6ZnO, and 8ZnO, respectively.
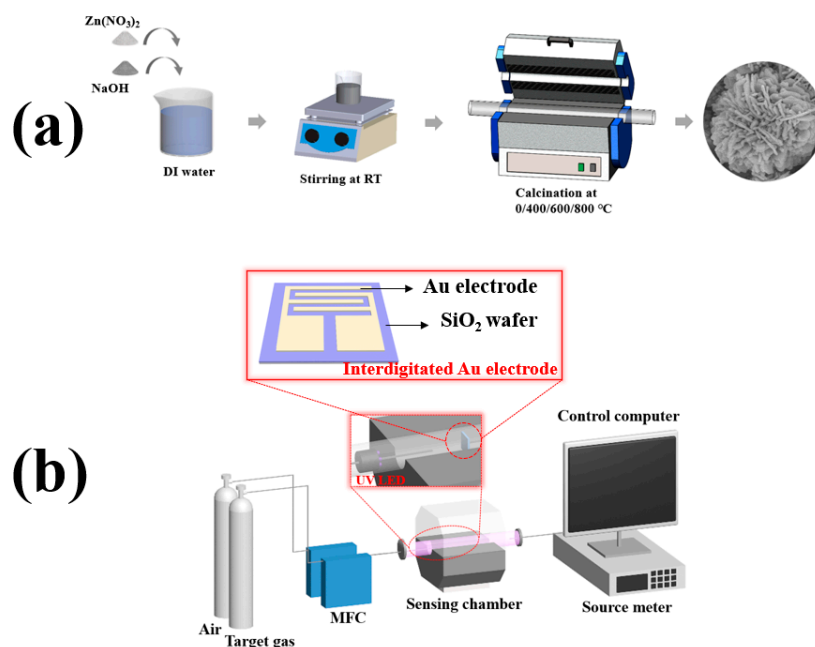

Figure 1. Schematic images of (**a**) the synthesis of the flower-like ZnO; (**b**) homemade gas sensing measurement system.

2.3. Characterization

Field-emission scanning electron microscopy (FESEM; HITACHI SU-8010) was used to examine the morphology and structure of the samples. X-ray diffraction (XRD; PANalytical

XPert-PRO MRD) with a Cu-Kα radiation source at λ = 1.54059 Å over the 2θ range of 20–80° and a scanning step size of 0.02° was utilized to investigate the crystal structure and phase composition of the samples. Field-emission transmission electron microscopy (FETEM; JEOL JEM-2100F) equipped with energy-dispersive X-ray spectroscopy (EDS; Oxford) was employed to further investigate the microstructure and elemental composition of the samples. X-ray photoelectron spectroscopy (XPS; ULVAC-PHI PHI 5000 Versa Probe II) was used to analyze the surface chemistry of the samples. Ultraviolet and visible spectrophotometry (UV–Vis; Agilent Cary-5000) was employed to study the optical properties of the samples. Specific surface area analysis (BET; BELSORP-max) was carried out to determine the surface area and pore size distribution of the samples.

2.4. Fabrication and Measurement of Gas Sensors

The structure of the gas sensor and measurement system is shown in Figure 1b. A suspension was obtained by dispersing 0.1 mg of the sample in 0.5 mL of ethanol. A drop of the suspension was placed onto the interdigitated Au electrode and then dried at 50 °C for 3 h. The distance between two neighboring Au electrodes was approximately 10 μm. The interdigitated Au electrode was mounted in the gas sensing chamber with provisions for gas inlet and outlet, and an 80 mW/cm^2, 365 nm UV lamp. To evaluate the gas sensing properties of the sensor, an MFC was used to control the flow of air and target gas into the sensing chamber. The external leads of the sensor were connected to a source meter (KEYSIGHT B2901A) with a data acquisition system that was controlled by a computer. The sensor was exposed to NO$_2$ gas, which is a common oxidizing gas, with concentrations ranging from 0.01 ppm to 1 ppm for 200 s. After the injection of target gas, synthetic air gas was introduced as the recovery time for the sensor, with a duration of 500 s. The response of the sensors (R) was calculated as R_a/R_g when the target gas was a reducing gas and R_g/R_a when the target gas was an oxidizing gas. The response and recovery times were measured until the resistance variation of the sensing chip reached 90% of the saturation value.

3. Experimental

3.1. Fabrication and Measurement of Gas Sensors

Figure 2 shows the FESEM images of flower-like ZnO synthesized in this study. The panoramic morphologies of 0ZnO, 4ZnO, and 6ZnO are presented in Figure 2a–g, demonstrating high yield and uniformity. Magnified FESEM images showing close observations of the nanostructures are presented in Figure 2b–h. Figure 2a,b depict 0ZnO, Figure 2c,d depict 4ZnO, and Figure 2e,f depict 6ZnO. These images reveal that the detailed morphology of flower-like ZnO consists of well-defined, flower-like, three-dimensional (3D) microstructures with diameters in the range of 1–2 μm. The flower-like ZnO structure is comprised of numerous closely packed nanosheets, each approximately 60 nm thick, that interconnect to form a network-like surface of the "flower". This structure generates a range of pores with varying sizes that may enhance the chemical properties of the material and provide more active sites for gas molecules to adhere to, facilitating gas adsorption. Figure 2g,h show that as the calcination temperature increases to 800 °C, the morphology changes from "flower" to an irregular shape. This is because the higher temperature afforded a more rapid nucleation rate, anisotropic growth on ZnO, and promoted the disorderly movement of the particles. As the temperature increases, the rapid formation of crystal nuclei leads to the phenomenon of "nuclear aggregation", resulting in aggregation among the crystal nuclei. The rate of particle aggregation is a crucial factor that affects the final morphology and structure of the products. The findings suggest that higher temperatures can lead to more severe agglomeration of ZnO particles, ultimately leading to a decrease in the specific surface area of the samples. Therefore, Figure 2h reveals that the calcination temperature is one of the essential factors that influence the surface morphology [32–34].
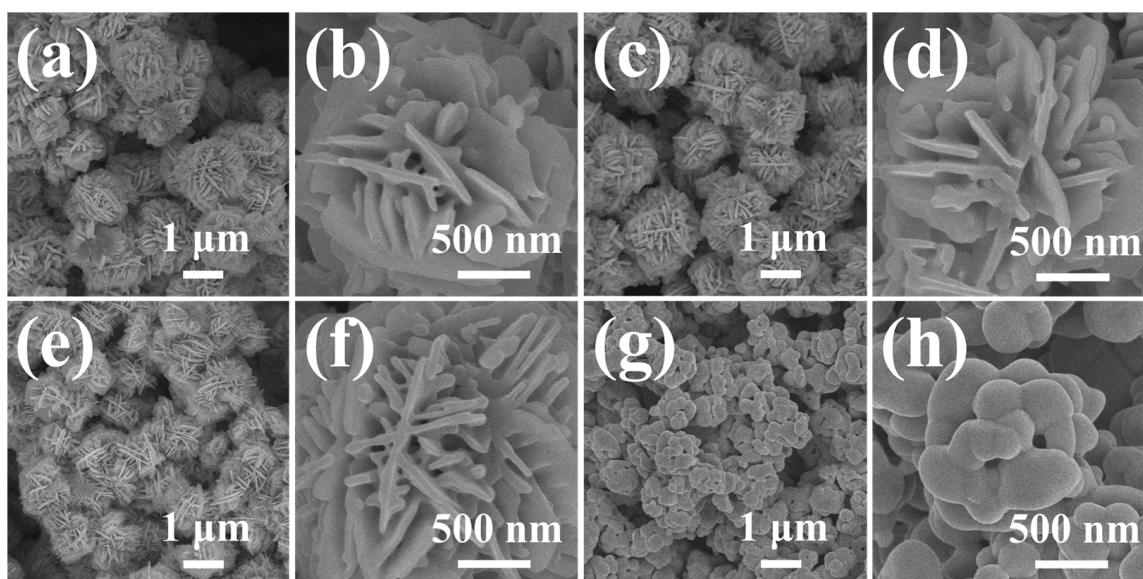
Figure 2. Low-magnification SEM images of the flower-like ZnO (**a**) before calcination, calcinated at (**c**) 400 °C, (**e**) 600 °C, and (**g**) 800 °C, (**b**,**d**,**f**,**h**) represent corresponding high-magnification SEM images.

Figure 3 shows the XRD patterns of the four samples calcined at different temperatures. The patterns show similar diffraction patterns, which mainly correspond to that of hexagonal-structured ZnO. As the calcination temperature increased, the intensities of the ZnO peaks gradually increased, and the corresponding half-widths of the peaks became narrower. The samples exhibited the narrowest half-width at 800 °C. According to the Scherrer formula:

$$D = 0.89\lambda / \beta \cos\theta \tag{1}$$

where λ, β, and θ represent the wavelength of X-ray radiation, full width at half maximum (FWHM), and diffraction angle of the peaks, respectively, the average crystallite sizes of the samples were estimated and are listed in Table S1. The crystallite sizes increased from 16.56 nm to 35.35 nm as the calcination temperature increased.
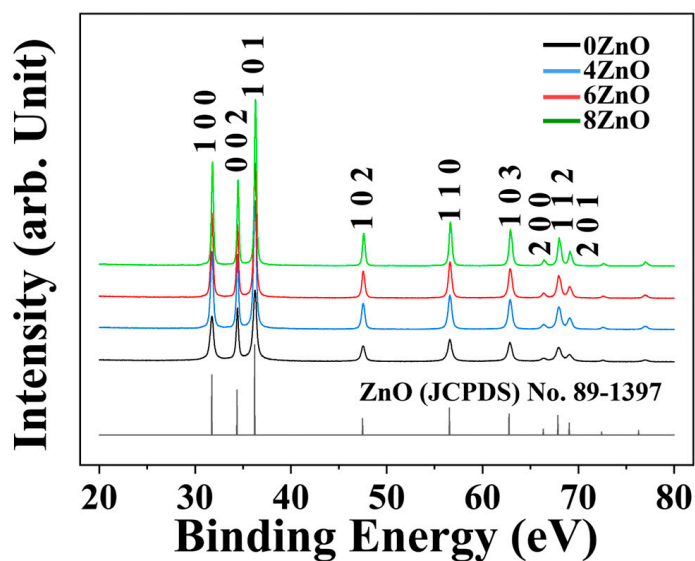

Figure 3. XRD patterns of the samples synthesized in this study.

FETEM observations were also performed to further investigate the interior and crystalline structure of the 6ZnO composites. The low magnification image in Figure 4a shows that the individual composites are assembled from nanosheets, and that their diameter is approximately 2 μm. The internal structure of the composites is broad, and the nanosheets are aggregates of 60 nm-thick layers as shown in the enlarged TEM image in Figure 4b. The high-resolution TEM image of a nanosheet from the ZnO structure in Figure 4c clearly reveals the crystalline structure with fringe spacing of 2.44 Å and 2.82 Å, corresponding to the lattice constant of the (101) and (100) planes of wurtzite ZnO, respectively. The corresponding selected area electron diffraction pattern (SAED) of the ZnO nanosheet is shown in Figure 4d. The point spots in the pattern are assigned to the (103), (002), and (104) lattice planes of ZnO, respectively. The morphology of ZnO was observed through a STEM image, revealing a flower-like structure. The elemental composition of ZnO was analyzed using EDX, and color mapping analysis was performed. The results shown in Figure 4e–g confirmed the presence of both Zn and O elements in the ZnO sample, and EDX mapping demonstrated a uniform distribution of Zn and O throughout the sample.
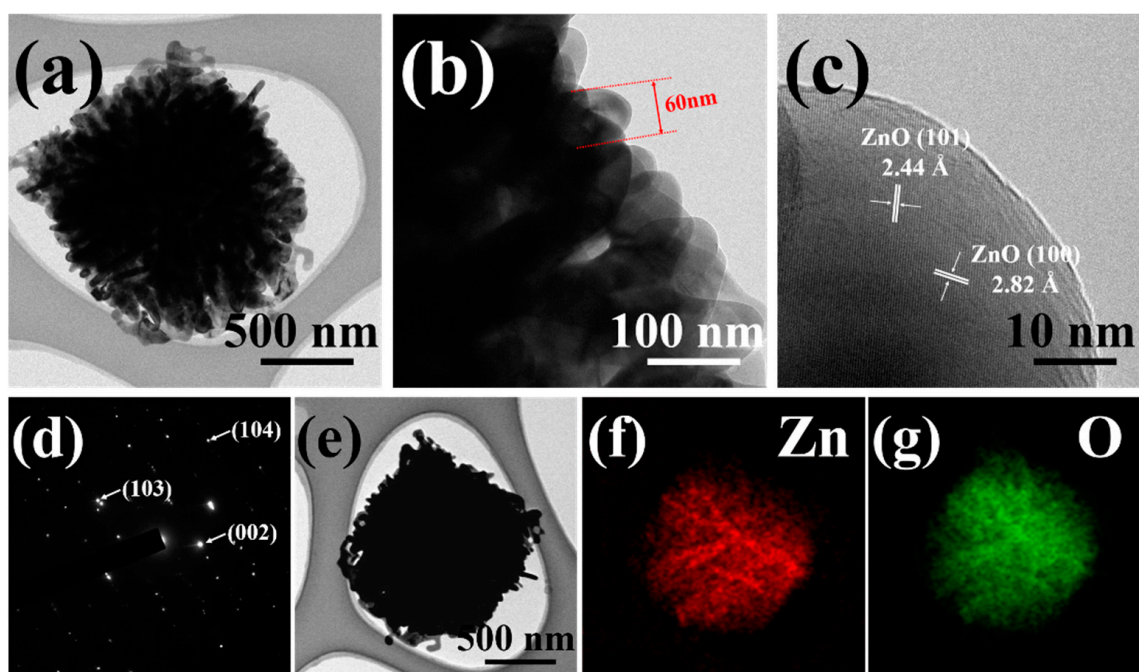

Figure 4. TEM images of 6ZnO: (**a**) low-magnification image showing its complete morphology; (**b**) the size of densely arranged nanosheet assembled flower-like ZnO; (**c**) an enlarged high-resolution image of the fringe patterns indicating its lattice planes; (**d**) its corresponding SEAD patterns; (**e**) STEM image of 6ZnO, and EDS elemental mapping profiles based on the STEM image of (**f**) Zn, and (**g**) O.

To investigate the surface composition and chemical states of the flower-like ZnO, XPS analysis was performed on samples synthesized in this study. The only peaks in the survey spectra that could not be attributed to Zn and O were located at 284.08 eV, which corresponded to the reference carbon (C 1s) material used for energy calibration [35], as shown in Figure 5a. Figure 5b clearly indicates that the binding energies of two peaks are located at ~1022 eV and ~1045 eV. The energy difference of 22.97 eV between the two peaks confirms the normal state of Zn^{2+}, which corresponds to $2p_{3/2}$ and Zn $2p_{1/2}$ peaks, respectively [36,37].
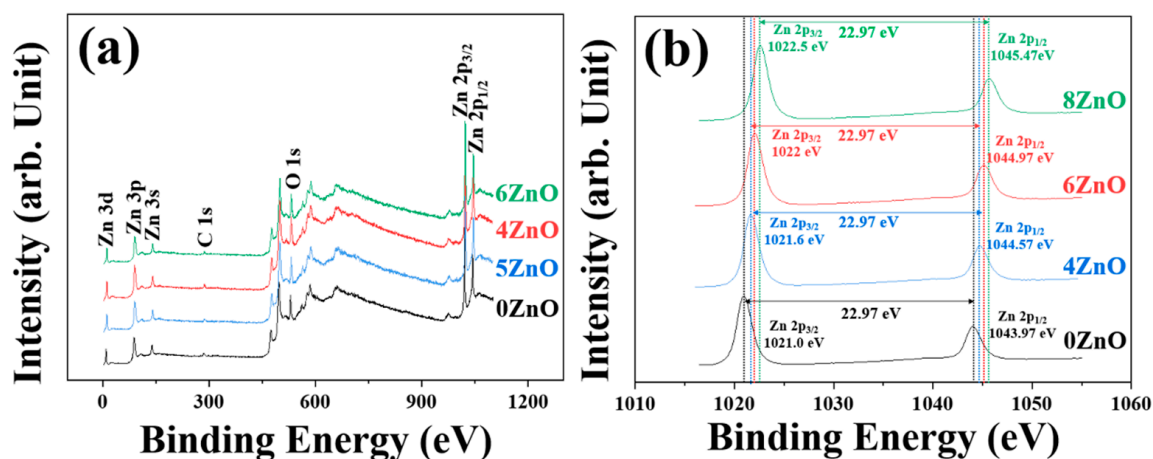
Figure 5. (**a**) XPS full-scan profiles of the flower-like ZnO at different calcination temperature and corresponding high-resolution XP spectra of (**b**) Zn 2p.

Figure 6 shows the XPS spectra of O 1s, which exhibits an asymmetric curvilinear shape that can be deconvoluted into three Gaussian sub-peaks according to their positions. These sub-peaks are attributed to lattice oxygen ($O_{lattice}$, ~530 eV), defective oxygen (O_{vac}, ~531 eV), and surface-adsorbed oxygen (O_{ads}, ~532 eV) [38,39], respectively. The $O_{lattice}$ ratio can reflect the crystallinity, which is an important parameter that affects the photocatalytic performance of the oxides. The $O_{lattice}$ ratio for 6ZnO is about 74.11%, which is higher than that of 0ZnO (72.65%) and 4ZnO (73.97%), and comparable to that of 8ZnO (76.18%). The $O_{lattice}$ ratio of flower-like ZnO increases with elevated temperature, indicating an improvement in its degree of crystallinity. This high crystallinity is known to enhance the separation efficiency of photogenerated electron-hole pairs, resulting in increased photocatalytic activity of the oxides [40,41]. Significant differences can be observed in the Zn 2p spectra of the three samples. The Zn $2p_{3/2}$ peaks are located at approximately 1021, 1021.6, 1022, and 1022.5 eV for 0ZnO, 4ZnO, 6ZnO, and 8ZnO, respectively. This shift to higher binding energy can be attributed to a decrease in the electron density surrounding the Zn atom. This phenomenon may be influenced by the amount of oxygen that is combined with Zn in the lattice, indicating that the increase in the $O_{lattice}$ content is responsible for the positive shift of the Zn 2p peaks [42,43]. An increase in the calcination temperature is also indicative of an enhancement in the crystallinity of ZnO, which aligns with the findings from the O 1s XRD investigations. Oxygen vacancy (O_{vac}) refers to the absence of, or missing of, an oxygen atom from its regular lattice site in a crystal structure. The intensity of this peak correlates with the number of oxygen vacancies, a higher content of O_{vac} allowing for greater adsorption and reduction of oxidizing gas molecules, resulting in higher sensor response values. The O_{vac} content of 6ZnO (16.09%) is higher than that of 0ZnO (14.57%), 4ZnO (13.78%), and 8ZnO (13.72%), indicating that 6ZnO should display the highest response. The presence of surface defects in flower-like ZnO enables it to adsorb and ionize more oxygen, resulting in a notable enhancement of the sensor response. In addition, elevated temperature is beneficial for enhancing the crystallinity of oxide materials, as well as for modifying the distribution of oxide species in ZnO [44–46]. During the high-temperature calcination process, the elevated temperatures create more favorable conditions for the release or diffusion of oxygen from the ZnO lattice. The increased thermal energy allows oxygen atoms to overcome activation barriers and migrate within the lattice, leading to the formation of oxygen vacancies. The high temperatures promote the breaking of oxygen bonds, resulting in the release of oxygen atoms from the crystal structure. Following calcination at 800 °C, the sample demonstrates an enhanced degree of crystallinity due to recrystallization, leading to a decrease in the presence of oxygen defects. Hence, we can conclude that calcination at a high temperature contributes

significantly to the positive activity and reuse performance of the photocatalyst and its gas sensing properties.
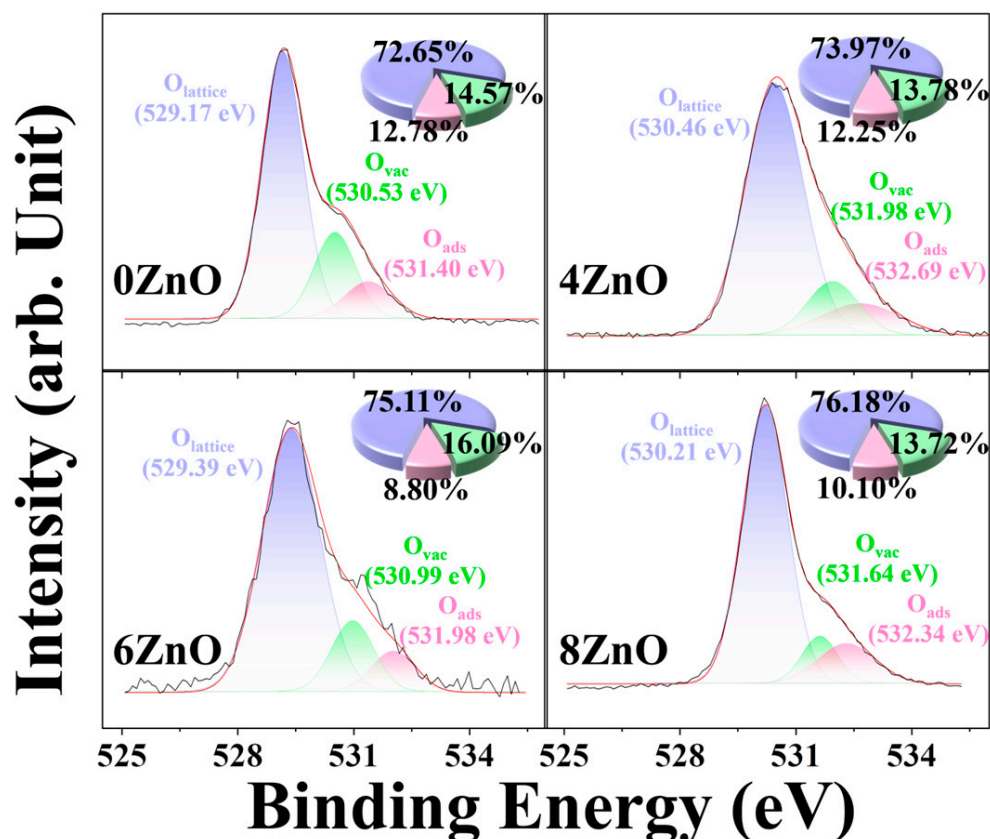

Figure 6. High-resolution XPS spectra and percentages of $O_{lattice}$, O_{vac}, and O_{ads} components for 0ZnO, 4ZnO, 6ZnO, and 8ZnO.

The specific surface area is a crucial factor in determining the material properties. A larger specific surface area is generally associated with more active sites participating in the reaction, which can lead to better performance of the material. To investigate the surface area of the flower-like ZnO in more detail, Brunauer–Emmett–Teller (BET) N_2 adsorption–desorption analysis was performed, as shown in Figure 7. The N_2 absorption–desorption isotherms, corresponding to specific surface areas and average pore size distribution were obtained by calculation. As presented, the isotherms of samples can be confirmed as "type-IV" isotherms. The H3 hysteresis loops demonstrated that all the as-obtained samples possessed mesoporous structure. The large surface area of flower-like ZnO is due to the growth between the interlayer of nanosheets. The specific surface areas of ZnO samples were observed by the BET method, and are 5.25 $m^2 \cdot g^{-1}$, 5.49 $m^2 \cdot g^{-1}$, 5.61 $m^2 \cdot g^{-1}$, and 2.01 $m^2 \cdot g^{-1}$, respectively. As the calcination temperature increased to 800 °C, the surface area of the flower-like ZnO decreased due to recrystallization of the body. Therefore, in the case of 8ZnO, its surface area is smaller than the other three samples. The pore size distribution of the flower-like ZnO is found to be within the range of 30–50 nm, with a small pore volume mainly attributed to slit pores. This suggests that the composite formed by ZnO sheets not only increases the specific surface area, but also generates more abundant pores or cracks, enabling greater diffusion and adsorption of gas molecules, which ultimately contributes to the improved gas sensing performance.
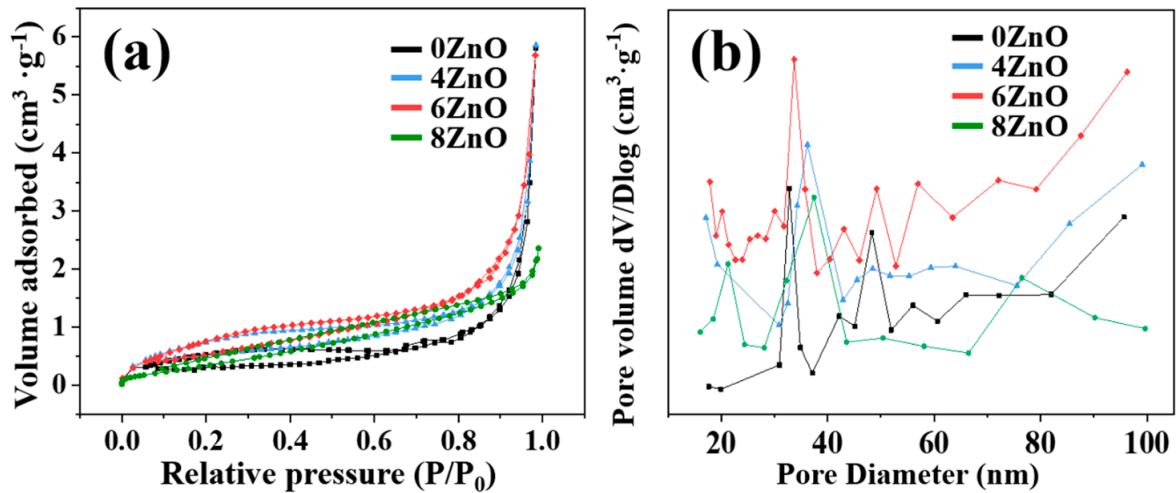
Figure 7. (**a**) N$_2$ adsorption–desorption isotherms and (**b**) pore diameter distributions of 0ZnO, 4ZnO, 6ZnO, and 8ZnO.

The UV–Vis absorption spectra were measured at room temperature to gain further insight into the changes in band gap in response to different calcination temperatures. Figure 8 shows the UV–Vis absorption spectra of all the samples. The flower-like ZnO samples exhibit intense absorption in the UV region (365 nm) and weak absorption in the visible light region. Compared to 0ZnO, the other three samples exhibit higher optical absorption, as evidenced by their higher absorption peaks. The bandgap energy of the samples was determined by plotting the curve of $(\alpha h\nu)^2$ as a function of photon energy ($h\nu$), according to Tauc's relation, as shown in the inset of Figure 8a:

$$(\alpha \, h \, \nu)^2 = A\left(h\nu - E_g\right) \tag{2}$$

where α is the absorption coefficient, $h\nu$ is the photon energy, A is the dimensional co-efficient, and E_g is the bandgap energy. The bandgap for 0ZnO (3.43 eV) is higher than those for 4ZnO (3.42 eV), 6ZnO (3.40 eV), and 8ZnO (3.39 eV). The bandgap values of the flower-like ZnO samples increase with decreasing calcination temperature. The bandgap for 0ZnO (3.43 eV) is the highest among the samples, while those for 4ZnO (3.42 eV), 6ZnO (3.40 eV), and 8ZnO (3.39 eV) are successively lower. The narrowed bandgaps may enhance the activation of electron migration by UV light, leading to an improvement in the photocatalytic activity.
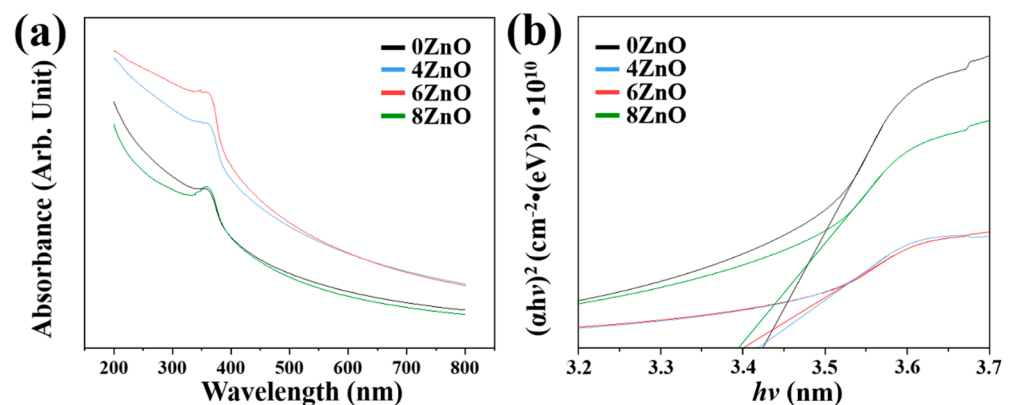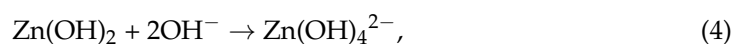

Figure 8. (**a**) UV–Vis absorption spectrum, and (**b**) plots of $(\alpha h\nu)^2$ versus photo $h\nu$ of 0ZnO, 4ZnO, 6ZnO, and 8ZnO.

3.2. The Formation Mechanism of Flower-like ZnO

We conducted experiments at different NaOH concentrations to study the formation of flower-like ZnO. Figure S1 shows FESEM images of the samples obtained at different stages of NaOH concentration. When 0.3 g NaOH was added, the reaction resulted in the rudiments of flower-like ZnO, which consisted of some incompact nanosheets, as shown in Figure S1a,b. We also observed that some tiny nanoparticles appeared on the surfaces of the nanosheets, which might provide growing points for other nanosheets in the next stage. When 0.6 g NaOH was added, as shown in Figure S1c,d, the sample obtained consisted of well-shaped flower-like structures with thin but larger sizes, assembled by numerous interleaving nanosheets. The morphology and size of ZnO remained almost constant as the concentration of NaOH increased, as illustrated in Figure 2a,b. Since no organic additives, templates, or surfactants were used in the reaction system, the key roles in the formation of flower-like ZnO are played by the concentrations of Zn^{2+} and OH^-. To explain the formation of flower-like ZnO, we propose the following mechanism, as shown in the schematic illustration of the formation process and mechanism in Figure S2. The growth process of flower-like ZnO in an alkaline solution generally follows the mechanism outlined below [47–49]:

$$Zn^{2+} + 2OH^- \rightarrow Zn(OH)_2, \tag{3}$$

$$Zn(OH)_2 + 2OH^- \rightarrow Zn(OH)_4{}^{2-}, \tag{4}$$

$$Zn(OH)_4{}^{2-} \rightarrow ZnO + 2H_2O + 2OH^-. \tag{5}$$

We propose that the growth process of flower-like ZnO occurs in two stages: the growth of ZnO sheet arrays and the formation of flower-like ZnO. The concentration of Zn^{2+} and OH^- ions serves as the primary driving force for the growth of ZnO crystals. When the concentration of reactants is high, initial homogeneous nucleation takes place, leading to the formation of a $Zn(OH)_2$ precipitate as illustrated in Equation (3). As more NaOH solution is added, the $Zn(OH)_2$ precipitate dissolves, yielding a homogeneous aqueous solution containing $Zn(OH)_4{}^{2-}$ ions, as demonstrated in Equation (4). The $Zn(OH)_4{}^{2-}$ ions undergo a dehydration reaction in situ, transforming into minuscule ZnO particles. As reactants are continuously supplied to the chemical environment, active sites on the surface of the initially formed ZnO aggregates undergo directional growth. In previous growth modes involving catalysts or substrates [50–52], hexagonal rods elongated along the c-axis were synthesized, as depicted in Figure S2, due to the intrinsic anisotropy in their growth rate, with $[0001] > [01\bar{1}0] > [000\bar{1}]$. In an alkaline solution with an exceptionally high concentration of OH^- ions, the positively charged (0001) plane absorbs excess OH^- ions, which stabilizes the structure of (0001) surfaces to some extent. The swift expansion along the $[01\bar{1}0]$ direction promotes selective development in the [0001] and $[01\bar{1}0]$ directions within the $\{2\bar{1}\bar{1}0\}$ plane, thus resulting in the generation of nanosheets on the exterior of the originally formed ZnO aggregation. As the reaction time progresses, the small and thin ZnO sheets continue to grow, and an increasing number of ZnO sheets form. The growth of ZnO sheets ceases when their diameters and thicknesses reach a certain value. Ultimately, the small ZnO sheets develop into larger ones, and the petal diameters tend to be remarkably uniform [53–55].

3.3. Gas Sensing Properties

The response of the sensors to 1 ppm of NO_2 at RT without and with UV irradiation is shown in Figure 9a. The 0ZnO, without UV irradiation does not show any response to 1 ppm of NO_2 at RT, and the other three samples have a very weak response (<2). The noise is strong with no saturation in response and recovery. In contrast, all four samples under UV irradiation at RT produced good saturation responses to 1 ppm of NO_2. The sensors with 6ZnO showed the highest response values to NO_2, followed by 4ZnO, 8ZnO, and 0ZnO. The dynamic response transients of 0ZnO, 4ZnO, 6ZnO, and 8ZnO to NO2 in

the concentration range from 0.01 ppm to 1 ppm at RT with UV irradiation are shown in Figure 9b. The response increased with the increasing NO_2 concentration, and the highest response of 6ZnO to 1 ppm NO_2 was 54.18, which was 3.58 times higher than that of 0ZnO. The response curves of these four sensors as a function of NO_2 concentration at RT with UV irradiation are shown in Figure 9c. These four sensors tend to rise with increasing NO_2 concentration, but 6ZnO exhibits a much higher increasing rate. From the linear fitted response versus NO_2 concentration relationship, the fitted curves of these four sensors exhibit linearity at low NO_2 concentrations ranging from 0.01 ppb to 1 ppm. The fitting functions are calculated as y = 13.798x + 1.9901, y = 40.152x + 1.9964, y = 51.701x + 2.6318, and y = 32.711x + 1.4691 for 0ZnO, 4ZnO, 6ZnO, and 8ZnO, respectively. The corresponding correlation coefficients, R^2, are 0.9792, 0.9967, 0.9998, and 0.9985 for the four samples, respectively. It is evident that 6ZnO exhibits the best linearity with respect to NO_2. To determine the detection limit of S2, we calculated the noise level before introducing the test gas by measuring the root-mean-square (RMS) deviation at the baseline. The theoretical limit of detection (LOD) can be calculated using the formula: [22,56,57].

$$\text{LOD} = \frac{3\text{RMS}_{\text{noise}}}{\text{m}} = 3\sqrt{S^2/N/m} \tag{6}$$

where m is the slope of the calibration curve, S is the standard deviation, and N is the number of data points. The results indicate that 6ZnO has the lowest LOD value among the tested samples. Figure 9d presents the response and recovery time for all of the sensors, and it is evident that the calcination process significantly reduces the response and recovery time of 4ZnO, 6ZnO, and 8ZnO. Among all the sensors, 6ZnO exhibits the shortest response and recovery time. Compared to 0ZnO, the response and recovery time of 6ZnO was reduced from 32 s and 339 s to 11 s and 93 s, respectively. Consequently, all subsequent experiments were performed using this sensor alone.
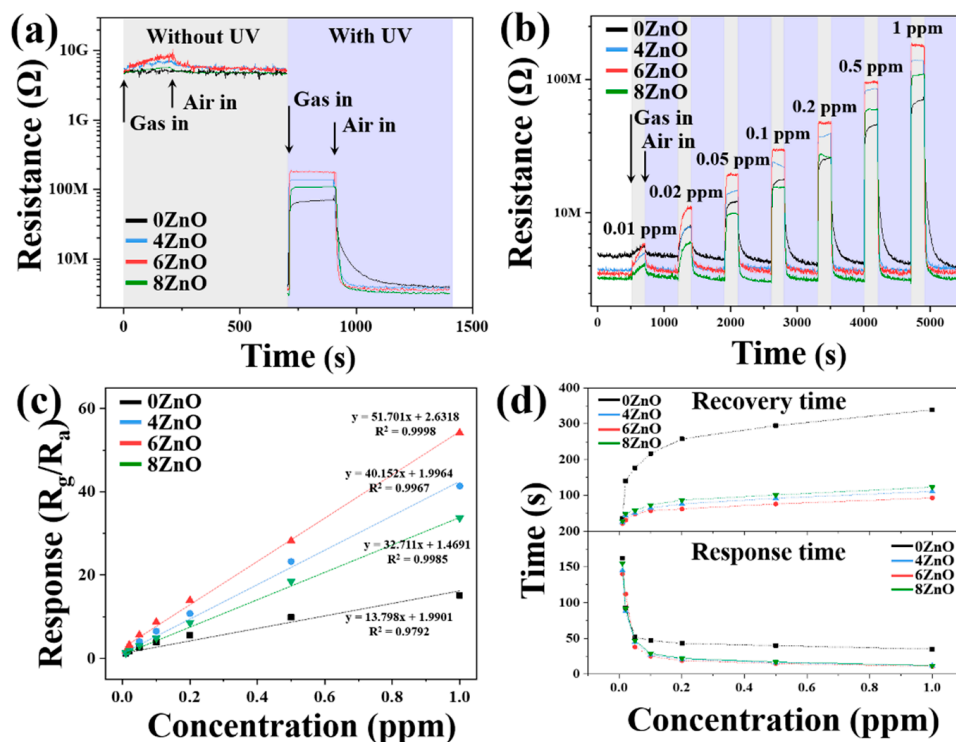

Figure 9. (**a**) The dynamic response transients of sensors to 1 ppm NO_2 gas in the dark and under 365 nm UV irradiation at RT; (**b**) dynamic response transients; (**c**) summarized response, and (**d**) response/recovery times of 0ZnO, 4ZnO, 6ZnO, and 8ZnO as a function of the NO_2 gas concentration under 365 nm UV irradiation at RT.

The impact of humidity on the 6ZnO sensor was studied by exposing it to 1 ppm of NO_2 at RT under varying humidity levels (0–80% RH), as illustrated in Figure 10a. The sensing curves revealed that, as the relative humidity increased, both the baseline resistance and response values of 6ZnO decreased. The decreased baseline resistance and response were associated with the adsorption of H_2O molecules to the surface of the material. In flower-like ZnO, the large specific surface area provides ample hydrophilic active sites for H_2O molecules to adsorb, thus reducing the number of active sites available for NO_2 molecules to adsorb. As the number of H_2O molecules increased, these molecules were more likely to capture the active sites of NO_2 molecules, resulting in a lower response [58–60]. In a high-moisture environment (80% RH), the sensor response dropped from 54.18 to 49.25. Selectivity is considered an important parameter for practical applications. The 6ZnO sensor was tested for various concentrations of interfering gases, such as 100 ppm of ethanol, acetone, benzene, xylene, toluene, and CO, 20 ppm of H_2S, and 500 ppm of H_2 at a working temperature of RT, as shown in Figure 10b. The flower-like ZnO sensor demonstrated a remarkable response to NO_2, surpassing the response of all other interfering gases even at lower NO_2 concentrations. These results suggest that the flower-like ZnO sensor has potential for selective detection of NO_2 at RT for quality monitoring. Additionally, the repeatability and long-term stability of the 6ZnO nanoplate-based sensors were investigated for their ability to detect 1 ppm of NO_2. As illustrated in Figure 10c,d, the sensor exhibited consistent performance after ten consecutive measurement cycles, confirming its excellent repeatability. Furthermore, the sensor's response values were consistent even after 30 days of testing at RT under UV illumination, with a deviation below 8%. These findings highlight the excellent long-term stability and repeatability of the flower-like ZnO-based sensor, demonstrating its potential for practical applications.
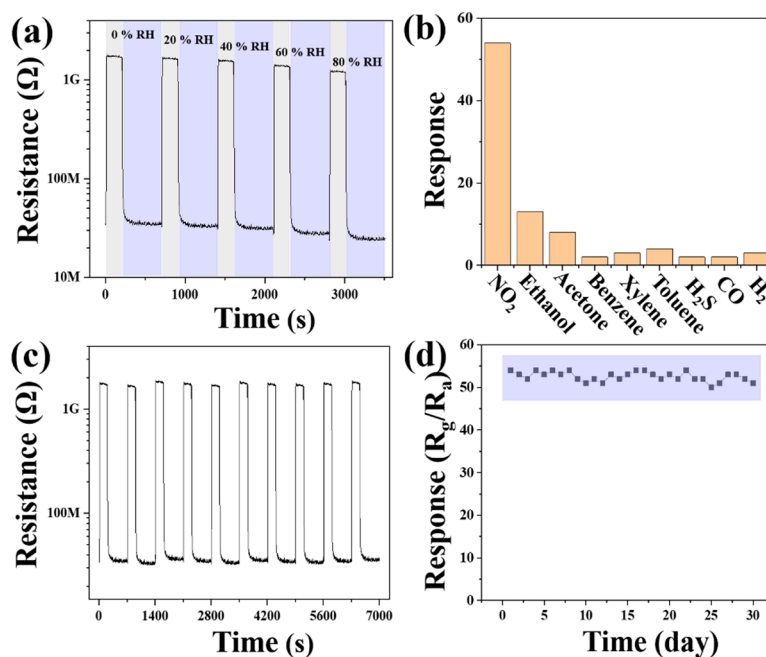

Figure 10. (**a**) Dynamic response transients of 6ZnO as a function of RH; (**b**) sensing responses of 6ZnO to various gases (NO_2, ethanol, acetone, benzene, p-xylene, toluene, H_2S, CO and H_2); (**c**) ten cycle repeatability to 1 ppm NO_2 gas, and (**d**) 30 days stability to 1 ppm NO_2 gas under 365 nm UV irradiation at RT.

A comparison of the NO_2 sensing performance of the flower-like ZnO sensor prepared in this work with other NO_2 sensors from the literature is summarized in Table 1 [61–66]. The 6ZnO sensor not only achieves low-concentration detection at room temperature, but also has a response that is significantly better than the other sensors.

Table 1. NO_2 response of ZnO-based gas sensors with different morphologies and the porous ZnO NSs gas sensor.

Material	Operating Temperature (°C)	Concentration (ppm)	Response	Refs.
Nanorods	RT	25	13	[61]
Hollow	200	1	15.3	[62]
Mesoporous	120	1	8.4	[63]
Nanorods	200	100	7.22	[64]
Nanosheets	RT	1	6	[65]
Spheres	RT	100	8.9	[66]
Flowers	RT	1	54.18	This work

4. Discussion

It is well known that, as a typical n-type metal oxide semiconductor, the gas sensing mechanism of the flower-like ZnO-based sensor is based on the changes in chemical resistance conductivity caused by the adsorption and desorption of the target gas molecules on the material's surface, as shown in Figure 11. When the flower-like ZnO is exposed to ambient air, oxygen molecules adsorb onto the surface and capture free electrons from the conduction band of the flower-like ZnO, generating surface oxygen species as follows [67]:
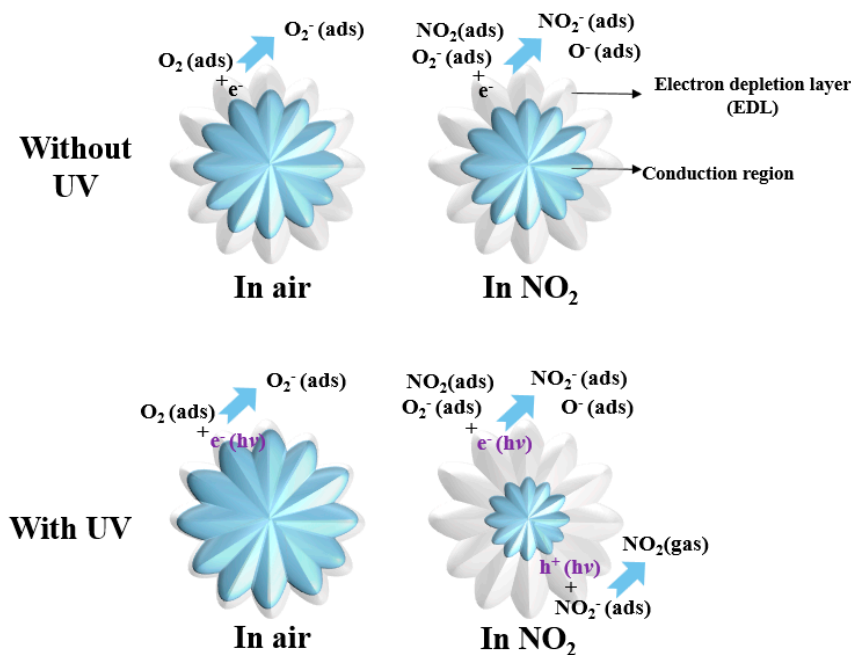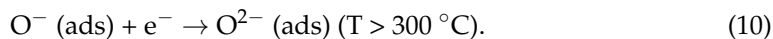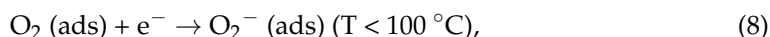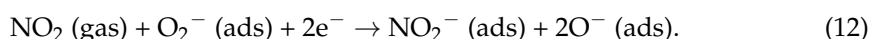
$$O_2 \ (g) \rightarrow O_2 \ (ads), \tag{7}$$

$$O_2 \ (ads) + e^- \rightarrow O_2^- \ (ads) \ (T < 100 \ °C), \tag{8}$$

$$O_2^- \ (ads) + e^- \rightarrow 2O^- \ (ads) \ (100 \ °C < T < 300 \ °C), \tag{9}$$

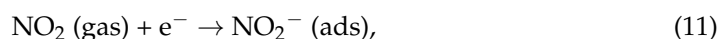$$O^- \ (ads) + e^- \rightarrow O^{2-} \ (ads) \ (T > 300 \ °C). \tag{10}$$

Figure 11. Schematic images of the electrical structure of flower-like ZnO.
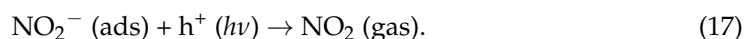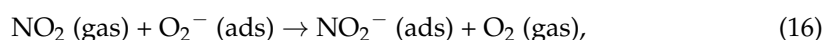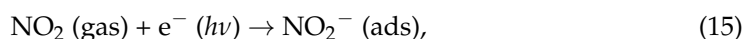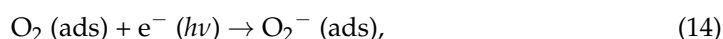
The sensing properties of these sensors were analyzed at RT in this study, so the O_2^- species dominated at RT, as shown in Equation (8). As a result, electrons were extracted from the surface of the flower-like ZnO, leading to the formation of an electron depletion layer (EDL) in air, which in turn increases the resistance of the material. When NO_2 gas is introduced, it can either be directly adsorbed onto the surface of the gas sensor or react with the already adsorbed oxygen species, as expressed below [68]:

$$NO_2 \text{ (gas)} + e^- \rightarrow NO_2^- \text{ (ads)}, \tag{11}$$

$$NO_2 \text{ (gas)} + O_2^- \text{ (ads)} + 2e^- \rightarrow NO_2^- \text{ (ads)} + 2O^- \text{ (ads)}. \tag{12}$$

The NO_2 molecules gain electrons, which widens the depletion layer and increases the resistance variation. When the flower-like ZnO is activated under UV light (365 nm), the energy of the UV light exceeds the bandgap of the material, generating massive electron-hole pairs, as shown in the following equation [69]:

$$h\nu \rightarrow e^- \ (h\nu) + h^+ \ (h\nu), \tag{13}$$
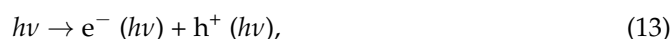
The photogenerated electrons transitioned from the valence band to the conduction band, further reducing the barrier height and resulting in a decrease in sensor resistance. There was competitive adsorption between NO_2 and O_2 molecules on the surface. As a large number of electrons were consumed in the gas-sensing reaction as shown in Equations (14) and (15), the carriers in the composite material decreased, and the resistance increased rapidly until it reached a stable value. When exposed to air, the photo-generated holes were beneficial in aiding the desorption of residual NO_2 species from the surface of the composite materials, as indicated in Equations (16) and (17). Furthermore, the high activity of the flower-like ZnO allowed for rapid reaction between photo-generated electrons and physically adsorbed oxygen molecules on the surface, resulting in the formation of new chemically adsorbed oxygen species. Both of these processes helped the sensor establish a new dynamic balance. Moreover, the participation of photo-generated electron-hole pairs in the recovery process contributed to a faster recovery speed of the sensor [70–72].

$$O_2 \text{ (ads)} + e^- \ (h\nu) \rightarrow O_2^- \text{ (ads)}, \tag{14}$$

$$NO_2 \text{ (gas)} + e^- \ (h\nu) \rightarrow NO_2^- \text{ (ads)}, \tag{15}$$

$$NO_2 \text{ (gas)} + O_2^- \text{ (ads)} \rightarrow NO_2^- \text{ (ads)} + O_2 \text{ (gas)}, \tag{16}$$

$$NO_2^- \text{ (ads)} + h^+ \ (h\nu) \rightarrow NO_2 \text{ (gas)}. \tag{17}$$

The enhanced NO_2 gas sensing properties of the present flower-like ZnO can be attributed to several aspects. Firstly, the crystallinity of 6ZnO is better than that of the other three samples, as confirmed by XRD and XPS analyses. The improved crystallinity of the prepared ZnO results in a stronger photoelectric effect, leading to a more significant modulation of resistance caused by the adsorption and desorption of gas molecules on the material's surface. Secondly, the crystal facets play a crucial role in the adsorption energy, and it was observed that the $\{2\bar{1}\bar{1}0\}$ facet has the highest adsorption energy, indicating that it is the most sensitive and active facet towards NO_2 molecules [73]. According to our analysis of the formation process of flower-like ZnO, the synthesized ZnO is composed of many nanosheets with $\{2\bar{1}\bar{1}0\}$ surfaces, so it has a more significant effect on the adsorption of NO_2 molecules, thereby improving the sensing response. Thirdly, the enhanced NO_2 gas sensing properties can be understood from the importance of surface defects. According to XPS analyses, the prepared 6ZnO sample has a higher density of oxygen vacancies than the

other three ZnO samples. These surface vacancies can serve as preferential adsorption sites for oxidizing gas molecules, which results in the absorption of more surface oxygen species on the ZnO surface. This, in turn, leads to an increased reaction of NO_2 molecules with the adsorbed surface oxygen species, resulting in an improved gas response. Finally, the unique flower-like structure of the as-prepared ZnO may also contribute to its enhanced NO_2 sensing properties. The porous structure observed in FESEM analysis provides numerous diffusion channels for NO_2 gas to access the internal surface of the material. This generates two electron-depleted layers on both surfaces of the individual ZnO nanosheet, offering more active sites necessary for NO_2 oxidation, thus leading to improved NO_2 sensing properties.

The flower-like ZnO was successfully synthesized using a simple chemical precipitation method at RT. The morphology of the ZnO was varied by adjusting the NaOH concentration without using catalyst or substrate. The high BET specific surface area increases the contact between the ZnO and target gas molecules, and the improved crystallinity enhances the photocatalytic performance of the material. These two factors allow 6ZnO, which has a higher BET specific surface area and crystallinity, to exhibit the best gas sensing performance among the four samples. For gas sensing, small grain size is required to provide a high surface area to bulk ratio, so the sensor samples were heat-treated below 600 °C. The 6ZnO sample showed a higher NO_2 gas sensing response of 54.18 compared to the other samples, for 1 ppm of NO_2. The response and recovery times for 1 ppm NO_2 were 11 and 93 s, respectively.

5. Conclusions

Flower-like ZnO was successfully synthesized at room temperature (RT) using a simple chemical precipitation method and adjusting the amount of NaOH added, without the use of any catalysts or substrates. The synthesized flower-like ZnO underwent calcination at different temperatures. ZnO calcined at 600 °C exhibited improved crystallinity, enhancing the material's photocatalytic performance. Additionally, it had a higher specific surface area compared to ZnO calcined at 800 °C, facilitating increased contact between ZnO and target gas molecules. These two factors resulted in the superior gas sensing performance of 6ZnO, which had the highest specific surface area and crystallinity of the four samples. In terms of gas sensing, the 6ZnO sample showed a higher response of 54.18 towards 1 ppm NO_2 gas at RT compared to the other samples. The response and recovery times for 1 ppm NO_2 were 11 and 93 s, respectively.

References

1. Vishnuraj, R.; Karuppanan, K.; Aleem, M.; Pullithadathil, B. Boosting the performance of NO_2 gas sensors based on n–n type mesoporous $ZnO@In_2O_3$ heterojunction nanowires: In situ conducting probe atomic force microscopic elucidation of room temperature local electron transport. *Nanoscale Adv.* **2020**, *2*, 4785. [CrossRef] [PubMed]
2. Kim, D.; Park, K.; Lee, S.; Fàbrega, C.; Prades, J.; Jang, J. Plasmon expedited response time and enhanced response in gold nanoparticles-decorated zinc oxide nanowire-based nitrogen dioxide gas sensor at room temperature. *J. Colloid Interface Sci.* **2021**, *582*, 658–668. [CrossRef] [PubMed]
3. Ou, J.; Ge, W.; Carey, B.; Daeneke, T.; Rotbart, A.; Shan, W.; Russo, S.; Li, Y.; Kalantar-Zadeh, K. Physisorption-based charge transfer in two-dimensional SnS_2 for selective and reversible NO_2 Gas Sensing. *ACS Nano* **2015**, *9*, 10313–10323. [CrossRef]
4. Liang, X.; Zhang, J.; Du, L.; Zhang, M. Effect of resonant tunneling modulation on ZnO/In_2O_3 heterojunction nanocomposite in efficient detection of NO_2 gas at room temperature. *Sens. Actuators B* **2021**, *329*, 129230. [CrossRef]
5. Kwon, S.; Kim, T.; Kim, S.; Ohm, S.; Kim, K. Ultraviolet light-emitting diode-assisted highly sensitive room temperature NO_2 gas sensors based on low-temperature solution-processed ZnO/TiO_2 nanorods decorated with plasmonic Au Nanoparticles. *Nanoscale* **2021**, *13*, 12177. [CrossRef]
6. Ying, S.; Wang, Y.; Wu, Z.; Huang, M.; Dong, L.; Zhao, J.; Peng, C. Highly-sensitive NO_2 gas sensors based on three-dimensional nanotube graphene and ZnO nanospheres nanocomposite at room temperature. *Appl. Surf. Sci.* **2021**, *566*, 150720. [CrossRef]
7. Xia, Y.; Zhou, L.; Yang, J.; Du, P.; Xu, L.; Wang, J. Highly sensitive and fast optoelectronic room-temperature NO_2 gas sensor based on ZnO nanorod-assembled macro-/mesoporous film. *ACS Appl. Electron. Mater.* **2020**, *2*, 580–589. [CrossRef]
8. Duoc, V.; Hung, C.; Nguyen, H.; Duy, N.; Hieu, N.; Hoa, N. Room temperature highly toxic NO_2 gas sensors based on rootstock/scion nanowires of SnO_2/ZnO, ZnO/SnO_2, SnO_2/SnO_2 and, ZnO/ZnO. *Sens. Actuators B* **2021**, *348*, 130652. [CrossRef]
9. Zhang, Q.; Pang, Z.; Hu, W.; Li, J.; Liu, Y.; Liu, Y.; Yu, F.; Zhang, C.; Xu, M. Performance degradation mechanism of the light-activated room temperature NO_2 gas sensor based on Ag-ZnO nanoparticles. *Appl. Surf. Sci.* **2021**, *541*, 148418. [CrossRef]
10. Yang, Z.; Jiang, L.; Wang, J.; Liu, F.; He, J.; Liu, A.; Lv, S.; You, R.; Yan, X.; Sun, P.; et al. Flexible resistive NO_2 gas sensor of three-dimensional crumpled MXene Ti_3C_2Tx/ZnO spheres for room temperature application. *Sens. Actuators B* **2021**, *326*, 128828. [CrossRef]
11. Kumar, R.; Murugesan, T.; Dash, A.; Hsu, C.; Gupta, S.; Manikandan, A.; Anbalagan, A.; Lee, C.; Tai, N.; Chueh, Y.; et al. Ultrasensitive and light-activated NO_2 gas sensor based on networked MoS_2/ZnO nanohybrid with adsorption/desorption kinetics study. *Appl. Surf. Sci.* **2021**, *536*, 147933. [CrossRef]
12. Xuan, J.; Zhao, G.; Sun, M.; Jia, F.; Wang, X.; Zhou, T.; Yin, G.; Liu, B. Low-temperature operating ZnO-based NO_2 sensors: A review. *RSC Adv.* **2020**, *10*, 39786. [CrossRef] [PubMed]
13. Öztürk, S.; Kılınç, N.; Taşaltın, N.; Öztürk, Z. A comparative study on the NO_2 gas sensing properties of ZnO thin films, nanowires and nanorods. *Thin Solid Film.* **2011**, *520*, 932–938. [CrossRef]
14. Liu, S.; Yu, B.; Zhang, H.; Fei, T.; Zhang, T. Enhancing NO_2 gas sensing performances at room temperature based on reduced graphene oxide-ZnO nanoparticles hybrids. *Sens. Actuators B* **2014**, *202*, 272–278. [CrossRef]
15. Shi, L.; Naik, A.; Goodall, J.; Tighe, C.; Gruar, R.; Binions, R.; Parkin, I.; Darr, J. Highly sensitive ZnO nanorod- and nanoprism-based NO_2 gas sensors: Size and shape control using a continuous hydrothermal pilot plant. *Langmuir* **2013**, *29*, 10603–10609. [CrossRef] [PubMed]
16. Patil, V.; Vanalakar, S.; Tarwal, N.; Patil, A.; Dongale, T.; Kim, J.; Patil, P. Construction of Cu doped ZnO nanorods by chemical method for Low temperature detection of NO_2 gas. *Sens. Actuators A* **2019**, *299*, 111611. [CrossRef]
17. Wang, Z.; Qian, X.; Yin, J.; Zhu, Z. Large-scale fabrication of tower-like, flower-like, and tube-like ZnO arrays by a simple chemical solution route. *Langmuir* **2004**, *20*, 3441–3448. [CrossRef] [PubMed]
18. Zhang, H.; Yang, D.; Ma, X.; Ji, Y.; Xu, J.; Que, D. Synthesis of flower-like ZnO nanostructures by an organic-free hydrothermal process. *Nanotechnology* **2004**, *15*, 622. [CrossRef]
19. Zheng, J.; Jiang, Q.; Lian, J. Synthesis and optical properties of flower-like ZnO nanorods by thermal evaporation method. *Appl. Surf. Sci.* **2011**, *257*, 5083–5087. [CrossRef]
20. Rai, P.; Raj, S.; Ko, K.; Park, K.; Yu, Y. Synthesis of flower-like ZnO microstructures for gas sensor applications. *Sens. Actuators B* **2013**, *178*, 107–112. [CrossRef]
21. Chen, M.; Wang, Z.; Han, D.; Gu, F.; Guo, G. High-sensitivity NO_2 gas sensors based on flower-like and tube-like ZnO nanomaterials. *Sens. Actuators B* **2011**, *157*, 565–574. [CrossRef]
22. Cai, Z.; Park, S. Ultrasensitive hydrogen sensor based on porous-structured Pd-decorated In_2O_3 nanoparticle-embedded SnO_2 nanofibers. *Sens. Actuators B* **2022**, *367*, 132090. [CrossRef]
23. Cai, Z.; Park, S. Highly selective acetone sensor based on Co_3O_4-decorated porous TiO_2 nanofibers. *J. Alloys Compd.* **2022**, *919*, 165875. [CrossRef]
24. Gu, C.; Cui, Y.; Wang, L.; Sheng, E.; Shim, J.; Huang, J. Synthesis of the porous NiO/SnO_2 microspheres and microcubes and their enhanced formaldehyde gas sensing performance. *Sens. Actuators B* **2017**, *241*, 298–307. [CrossRef]
25. Zhang, Y.; Li, D.; Qin, L.; Liu, D.; Liu, Y.; Liu, F.; Song, H.; Wang, Y.; Lu, G. Preparation of Au-loaded TiO_2 pecan-kernel-like and its enhanced toluene sensing performance. *Sens. Actuators B* **2018**, *255*, 2240–2247. [CrossRef]
26. Yang, C.; Li, Q.; Tang, L.; Xin, K.; Bai, A.; Yu, Y. Synthesis, photocatalytic activity, and photogenerated hydroxyl radicals of monodisperse colloidal ZnO nanospheres. *Appl. Surf. Sci.* **2015**, *357*, 1928–1938. [CrossRef]

27. Ba-Abbad, M.; Kadhum, A.; Mohamad, A.; Takriff, M.; Sopian, K. The effect of process parameters on the size of ZnO nanoparticles synthesized via the sol–gel technique. *J. Alloys Compd.* **2013**, *550*, 63–70. [CrossRef]
28. Wang, P.; Wang, S.; Kang, Y.; Sun, Z.; Wang, X.; Meng, Y.; Hong, M.; Xie, W. Cauliflower-shaped Bi$_2$O$_3$eZnO heterojunction with superior sensing performance towards ethanol. *J. Alloys Compd.* **2021**, *854*, 157152. [CrossRef]
29. Li, Q.; Chen, D.; Miao, J.; Lin, S.; Yu, Z.; Cui, D.; Yang, Z.; Chen, X. Highly sensitive sensor based on ordered porous ZnO nanosheets for ethanol detecting application. *Sens. Actuators B* **2021**, *326*, 128952. [CrossRef]
30. Gaiardo, A.; Fabbri, B.; Giberti, A.; Guidi, V.; Bellutti, P.; Malagù, C.; Valt, M.; Pepponi, G.; Gherardi, S.; Zonta, G.; et al. ZnO and Au/ZnO thin films: Room-temperature chemoresistive properties for gas sensing applications. *Sens. Actuators B* **2016**, *237*, 1085–1094. [CrossRef]
31. Cai, Z.; Kim, K.; Park, S. Room temperature detection of NO$_2$ gas under UV irradiation based on Au nanoparticle-decorated porous ZnO nanowires. *J. Mater. Res. Technol.-JMRT* **2020**, *9*, 16289–16302. [CrossRef]
32. Saravanan, R.; Thirumal, E.; Gupta, V.; Narayanan, V.; Stephen, A. The photocatalytic activity of ZnO prepared by simple thermal decomposition method at various temperatures. *J. Mol. Liq.* **2013**, *177*, 394–401. [CrossRef]
33. Wang, G.; Zhang, W.; Lian, H.; Jiang, D.; Wu, T. Effect of calcination temperatures and precipitant on the catalytic performance of Au/ZnO catalysts for CO oxidation at ambient temperature and in humid circumstances. *Appl. Catal. A-Gen.* **2003**, *239*, 1–10. [CrossRef]
34. Parra, M.; Haque, F. Aqueous chemical route synthesis and the effect of calcination temperature on the structural and optical properties of ZnO nanoparticles. *J. Mater. Res. Technol.-JMRT* **2014**, *3*, 363–369. [CrossRef]
35. Cai, Z.; Park, S. Synthesis of Pd nanoparticle-decorated SnO$_2$ nanowires and determination of the optimum quantity of Pd nanoparticles for highly sensitive and selective hydrogen gas sensor. *Sens. Actuators B* **2020**, *322*, 128651. [CrossRef]
36. Nakate, U.; Ahmad, R.; Patil, P.; Wang, Y.; Bhat, K.; Mahmoudi, T.; Yu, Y.; Suh, E.; Hahn, Y. Improved selectivity and low concentration hydrogen gas sensor application of Pd sensitized heterojunction n-ZnO/p-NiO Nanostructures. *J. Alloys Compd.* **2019**, *797*, 456–464. [CrossRef]
37. Girija, K.; Somasundaram, K.; Topkar, A.; Vatsa, R. Highly selective H$_2$S gas sensor based on Cu-doped ZnO nanocrystalline films deposited by RF magnetron sputtering of powder target. *J. Alloys Compd.* **2016**, *684*, 15–20. [CrossRef]
38. Cai, Z.; Park, S. A superior sensor consisting of porous, Pd nanoparticle–decorated SnO$_2$ nanotubes for the detection of ppb-level hydrogen gas. *J. Alloys Compd.* **2022**, *907*, 164459. [CrossRef]
39. Li, S.; Zhang, L.; Zhu, M.; Ji, G.; Zhao, L.; Yin, Y.; Bie, L. Acetone sensing of ZnO nanosheets synthesized using room-temperature precipitation. *Sens. Actuators B* **2017**, *249*, 611–623. [CrossRef]
40. Wang, Y.; Li, X.; Wang, N.; Quan, X.; Chen, Y. Controllable synthesis of ZnO nanoflowers and their morphology-dependent photocatalytic activities. *Sep. Purif. Technol.* **2008**, *62*, 727–732. [CrossRef]
41. Baradaran, M.; Ghodsi, F.; Bittencourt, C.; Llobet, E. The role of Al concentration on improving the photocatalytic performance of nanostructured ZnO/ZnO:Al/ZnO multilayer thin films. *J. Alloys Compd.* **2019**, *788*, 289–301. [CrossRef]
42. Liu, J.; Zhang, L.; Fan, J.; Zhu, B.; Yu, J. Triethylamine gas sensor based on Pt-functionalized hierarchical ZnO microspheres. *Sens. Actuators B* **2021**, *331*, 129425. [CrossRef]
43. Na, H.; Zhang, X.; Zhang, M.; Deng, Z.; Cheng, X.; Huo, L.; Gao, S. A fast response/recovery ppb-level H$_2$S gas sensor based on porous CuO/ZnO heterostructural tubule via confined effect of absorbent cotton. *Sens. Actuators B* **2019**, *297*, 126816. [CrossRef]
44. Wang, J.; Deng, J.; Li, Y.; Yuan, H.; Xu, M. ZnO nanocrystal-coated MoS$_2$ nanosheets with enhanced ultraviolet light gas sensitive activity studied by surface photovoltage technique. *Ceram. Int.* **2020**, *46*, 11427–11431. [CrossRef]
45. Hong, Y.; Tian, C.; Jiang, B.; Wu, A.; Zhang, Q.; Tian, G.; Fu, H. Facile synthesis of sheet-like ZnO assembly composed of small ZnO particles for highly efficient photocatalysis. *J. Mater. Chem. A* **2013**, *1*, 5700–5708. [CrossRef]
46. Jian, S.; Tian, Z.; Hu, J.; Zhang, K.; Zhang, L.; Duan, G.; Yang, W.; Jiang, S. Enhanced visible light photocatalytic efficiency of La-doped ZnO nanofibers via electrospinning-calcination technology. *Adv. Powder Mater.* **2022**, *1*, 100004. [CrossRef]
47. Chakraborty, S.; Kole, A.; Kumbhakar, P. Room temperature chemical synthesis of flower-like ZnO nanostructures. *Mater. Lett.* **2012**, *67*, 362–364. [CrossRef]
48. Ghosh, R.; Kundu, S.; Majumder, R.; Chowdhury, M. Hydrothermal synthesis and characterization of multifunctional ZnO Nanomaterials. *Mater. Today Proc.* **2020**, *26*, 77–81. [CrossRef]
49. Li, P.; Liu, H.; Zhang, Y.; Wei, Y.; Wang, X. Synthesis of flower-like ZnO microstructures via a simple solution route. *Mater. Chem. Phys.* **2007**, *106*, 63–69. [CrossRef]
50. Shi, R.; Yang, P.; Dong, X.; Ma, Q.; Zhang, A. Growth of flower-like ZnO on ZnO nanorod arrays created on zinc substrate through low-temperature hydrothermal synthesis. *Appl. Surf. Sci.* **2013**, *264*, 162–170. [CrossRef]
51. Ahsanulhaq, Q.; Kim, S.; Kim, J.; Hahn, Y. Structural properties and growth mechanism of flower-like ZnO structures obtained by simple solution method. *Mater. Res. Bull.* **2008**, *43*, 3483–3489. [CrossRef]
52. Li, B.; Wang, Y. Facile synthesis and enhanced photocatalytic performance of flower-like ZnO hierarchical microstructures. *J. Phys. Chem. C* **2010**, *114*, 890–896. [CrossRef]
53. Han, Z.; Liao, L.; Wu, Y.; Pan, H.; Shen, S.; Chen, J. Synthesis and photocatalytic application of oriented hierarchical ZnO flower-rod architectures. *J. Hazard. Mater.* **2012**, *217–218*, 100–106. [CrossRef] [PubMed]
54. Li, Y.; Yu, H.; Yang, Y.; Dong, X. Fabrication of 3D ordered mesoporous ball-flower structures ZnO material with the excellent gas sensitive property. *Sens. Actuators B* **2019**, *300*, 127050. [CrossRef]

55. Pan, L.; Muhammad, T.; Ma, L.; Huang, Z.; Wang, S.; Wang, L.; Zou, J.; Zhang, X. MOF-derived C-doped ZnO prepared via a two-step calcination for efficient photocatalysis. *Appl. Catal. B-Environ.* **2016**, *189*, 181–191. [CrossRef]

56. Tang, W.; Chen, Z.; Song, Z.; Wang, C.; Wan, Z.; Chan, C.; Chen, Z.; Ye, W.; Fan, Z. Microheater integrated nanotube array gas sensor for parts-per-trillion level gas detection and single sensor-based gas discrimination. *ACS Nano* **2022**, *16*, 10968–10978. [CrossRef]

57. Wu, J.; Tao, K.; Miao, J.; Norford, L. Improved selectivity and sensitivity of gas sensing using a 3D reduced graphene oxide hydrogel with an integrated microheater. *ACS Appl. Mater. Interfaces* **2015**, *7*, 27502–27510. [CrossRef]

58. Sanger, A.; Kang, S.; Jeong, M.; Kim, C.; Baik, J.; Choi, K. All-transparent NO_2 gas sensors based on freestanding Al-doped ZnO nanofibers. *ACS Appl. Electron. Mater.* **2019**, *1*, 1261–1268. [CrossRef]

59. Lu, G.; Xu, J.; Sun, J.; Yu, Y.; Zhang, Y.; Liu, F. UV-enhanced room temperature NO_2 sensor using ZnO nanorods modified with SnO_2 nanoparticles. *Sens. Actuators B* **2012**, *162*, 82–88. [CrossRef]

60. Park, S.; An, S.; Mun, Y.; Lee, C. UV-enhanced NO_2 gas sensing properties of SnO_2-Core/ZnO-shell nanowires at room temperature. *ACS Appl. Mater. Interfaces* **2013**, *5*, 4285–4292. [CrossRef]

61. Feng, C.; Wen, F.; Ying, Z.; Li, L.; Zheng, X.; Zheng, P.; Wang, G. Polypeptide-assisted hydrothermal synthesis of ZnO for room temperature NO_2 gas sensor under UV illumination. *Chem. Phys. Lett.* **2020**, *754*, 137745. [CrossRef]

62. Minh, L.; Thu, P.; Thanh, B.; Hanh, N.; Hanh, D.; Toan, N.; Hung, C.; Duy, N.; Tong, P.; Hoa, N. Hollow ZnO nanorices prepared by a simple hydrothermal method for NO_2 and SO_2 gas sensors. *RSC Adv.* **2021**, *11*, 33613. [CrossRef] [PubMed]

63. Xing, J.; Liu, Z.; Zhou, J.; Wang, Q.; Geng, Y.; Du, Y.; Pan, Q. Mesostructure Carbon-Templated synthesis of mesoporous ZnO by a nanocasting route for NO_2 sensing. *Mater. Lett.* **2019**, *244*, 182–185. [CrossRef]

64. Navale, Y.; Navale, S.; Ramgir, N.; Stadler, F.; Gupta, S.; Aswal, D.; Patil, V. Zinc oxide hierarchical nanostructures as potential NO_2 sensors. *Sens. Actuators B* **2017**, *251*, 551–563. [CrossRef]

65. Yan, D.; Hu, M.; Li, S.; Liang, J.; Wu, Y.; Ma, S. Electrochemical deposition of ZnO nanostructures onto porous silicon and their enhanced gas sensing to NO_2 at room temperature. *Electrochim. Acta* **2014**, *115*, 297–305. [CrossRef]

66. Liu, X.; Sun, J.; Zhang, X. Novel 3D graphene aerogel–ZnO composites as efficient detection for NO2 at room temperature. *Sens. Actuators B* **2015**, *211*, 220–226. [CrossRef]

67. Cai, Z.; Goo, E.; Park, S. Synthesis of tin dioxide (SnO_2) hollow nanospheres and its ethanol-sensing performance augmented by gold nanoparticle decoration. *J. Alloys Compd.* **2021**, *883*, 160868. [CrossRef]

68. Chen, M.; Wang, Z.; Han, D.; Gu, F.; Guo, G. Porous ZnO Polygonal Nanoflakes: Synthesis, Use in High-Sensitivity NO_2 Gas Sensor, and Proposed Mechanism of Gas Sensing. *J. Phys. Chem. C* **2011**, *115*, 12763–12773. [CrossRef]

69. Yang, Y.; Wu, S.; Cao, Y.; Li, S.; Xie, T.; Lin, Y.; Li, Z. A highly efficient room-temperature formaldehyde gas sensor based on a Ni-doped ZnO hierarchical porous structure decorated with NiS illuminated by UV light. *J. Alloys Compd.* **2022**, *920*, 165850. [CrossRef]

70. Nakarungsee, P.; Srirattanapibul, S.; Issro, C.; Tang, I.; Thongmee, S. High performance Cr doped ZnO by UV for NH_3 gas sensor. *Sens. Actuators A* **2020**, *314*, 112230. [CrossRef]

71. Zhou, Y.; Wang, Y.; Wang, Y.; Li, X.; Guo, Y. The impact of carrier gas on room-temperature trace nitrogen dioxide sensing of ZnO nanowire-integrated film under UV illumination. *Ceram. Int.* **2020**, *46*, 16056–16061. [CrossRef]

72. Han, C.; Li, X.; Liu, Y.; Li, X.; Shao, C.; Ri, J.; Ma, J.; Liu, Y. Construction of In_2O_3/ZnO yolk-shell nanofibers for room-temperature NO_2 detection under UV illumination. *J. Hazard. Mater.* **2021**, *403*, 124093. [CrossRef] [PubMed]

73. Geng, X.; Lu, P.; Zhang, C.; Lahem, D.; Olivier, M.; Debliquy, M. Room-temperature NO_2 gas sensors based on rGO@ZnO_{1-x} composites: Experiments and molecular dynamics simulation. *Sens. Actuators B* **2019**, *282*, 690–702. [CrossRef]